ANL/FPP/TM-268

ARGONNE NATIONAL LABORATORY
9700 South Cass Avenue
Argonne, Illinois 60439-4801

MODELLING EROSION DAMAGE FROM LOW-ENERGY PLASMA GUN SIMULATIONS OF DISRUPTIONS

by

David A. Ehst
Fusion Power Program/Engineering Physics Division

Ahmed Hassanein
Fusion Power Program/Energy Technology Division

October 1993

MASTER

TABLE OF CONTENTS

LIST OF FIGURES

LIST OF TABLES

MODELLING EROSION DAMAGE FROM LOW-ENERGY PLASMA GUN SIMULATIONS OF DISRUPTIONS

David A. Ehst and Ahmed Hassanein

ABSTRACT

Energy transfer to material surfaces is dominated by photon radiation through low temperature plasma vapors if tokamak disruptions are due to low kinetic energy particles ($\lesssim 100$ eV). Simple models of radiation transport are derived and incorporated into a fast-running computer routine to model this process. The results of simulations are in good agreement with plasma gun erosion tests on several metal targets.

1.   Vapor Shield Model and Code Description

Ablation of material surfaces due to thermal disruptions in large tokamaks is an increasing concern as we start detailed engineering design of ignited machines like ITER. Bench tests of candidate materials have been pursued with high intensity pulsed power sources -- lasers, electron beams, and plasma guns -- capable of delivering reactor-relevant heat loads, $\gtrsim 10$ MJ/m^2 in $\lesssim 1$ ms. However, pulsed power from these different sources results in distinctively different amounts of erosion. As seen in Table I the erosion damage due to electron beams is significantly less than expected from an unshielded heat pulse. This is evidence that the ablated vapor itself can absorb a substantial amount of energy, which serves to reduce the heat flux to the material surface. Yet the protective factor for plasma guns is much higher than for electron beams. This behavior is due to qualitative differences between the sources. Electrons at 60 KeV suffer slowing down due to the stopping power of vaporized atoms, but they nevertheless penetrate vapor clouds and can deliver a reduced but substantial amount of energy to the surface. Plasma guns however produce a much higher source current density but at very low ($\lesssim 1$ KeV) particle kinetic energy. Such low energy particles easily suffer collisional scattering and thermalize without streaming through the vapor cloud; energy transport through the vapor is accomplished mainly by photon radiation. The purpose of this report is to present a simple theory of vapor shielding accompanying plasma gun pulses and

to document tests of a computer routine, DESIRE, in which our theory is compared to experimental data. In the future, refinements of our model will enable us to predict the disruption erosion resistance of candidate plasma-facing materials for large tokamaks.

Table I
Thermal Erosion (μm) Due to Heat Pulses (0.10 ms) Delivered to Tungsten

Source	Energy Density (MJ/m^2)	
	4.0	12.0
Unshielded[a]	28.	103.
Electron beam[b]	10.	-----
Plasma gun[c]	<0.3	1.0

a- Calculated from A*THERMAL without vapor shielding; does not include melting.
b- 60 KeV beam; Efremov Inst. (V. Barabash, et al.) experiment.
c- 30 eV hydrogen; Efremov Inst. (V. Barabash, et al.) experiment.

Our model presently is limited by a variety of simplifying but reasonable assumptions. We assume the incoming plasma has particle kinetic energies $\lesssim 50$ eV, and our examples consider only a pure hydrogen source. The plasma from the gun piles up in front of the surface and forms a *source* vapor which radiates over a broad spectrum. A second plasma evolves as the material surface evaporates; this *target* vapor partly absorbs the power radiated by the source vapor and transmits part of the power to the surface. A schematic of this two-zone model is in Fig. 1. On the rather slow time scale under consideration ($\gtrsim 10^{-7}$ s) the two vapors are in local thermodynamic equilibrium, and we idealize the zones as each having uniform properties -- temperature (θ), density (n), charge state (Z), and degree of ionization (Φ). There is no mixing between zones and no thermal conduction. Compared to many-zone hydrodynamic treatments this approach may appear crude, but, as we shall see, this method yields results in remarkably good agreement with experiments.

2

Although other cross sections are possible we presently consider circular plasma beams of diameter d; open shutter photography [Barabash] shows the source plasma from a gun is well columnated. Under extreme circumstances the two vapors, of thickness Λ_S and Λ_T, may expand and contact external surfaces, such as the gun electrodes, at a distance d_G. Such surfaces can serve as particle and energy sinks, but this possibility is not implemented in the examples that follow.

In applying energy conservation to the two-zone system two important features are incorporated. First, the vapors, especially the source vapor, have significant heat capacities which store much of the externally supplied energy density. Second, both vapors radiate profusely in directions away from the material surface. Thus the source vapor radiates "backward" towards the external heat source, and both zones radiate "sideways" (parallel to the material surface); these constitute large energy sinks, limiting the energy ultimately deposited on the material surface.

1.1   Vapor Shielding Physics and DESIRE Code Calculations

The flow chart for DESIRE is shown in Fig. 2; the three blocks of code, APHYSICS, OPTCDPTH, and STATE, can run as a subroutine to A*THERMAL [Hassanein] or in an approximate stand-alone package. The actual equations are detailed in Appendix A of this report, and in this section we give a brief discussion of the physics models. The following sequence of subsections refers to the bracketed numbers in the flow chart. Also note that most of the calculations are done twice, once for the source vapor (subscript S) and once for the target vapor (subscript T).

The object of our calculation is N_T, the line-averaged density of target atoms vaporized during the pulse, from which the surface ablation depth is inferred. Other principal variables, updated at each time step, are, for both vapor species, U (line-averaged energy density), θ (temperature), Φ (degree of ionization), Z (effective charge), and n (density).

1.1.1   Source current density. We assume a fully ionized external plasma source; the input energy density, as measured in calorimetry experiments

3

[Suzuki], includes the ionization energy, $\chi_H = 13.58$ eV, consumed in producing the source plasma. The current density J_S is related to the input power density q_0 as given by Eq. (A1).

1.1.2 Line-averaged source density.

We find N_S by integrating J_S each time step. Additionally, particle losses are permitted from the source vapor (if the source vapor thickness, Λ_S, expands too far) but are not considered in the examples in this report.

1.1.3 Pressure balance.

Optical depth computations require knowledge of (volumetric) density as well as line average density. Our treatment considers the ion momentum input from the external source as an impulse which provides instantaneous pressure equilibration between the source and target vapors. From this external pressure, Π, the density n is found [Eqs. (A3) - (A6)], using the previous time step's values for θ, Φ, and Z. The target vapor compression resulting from the external momentum input yields values of n_T much larger than expected from free expansion of the ablated material. The resulting zone thickness for each vapor is given simply by $\Lambda = N / n$.

1.1.4 Optical depth from free-free, (inverse) Bremsstrahlung.

The opacity is calculated at one hundred wavelengths, centered on the peak emission of the source vapor, which is the hotter plasma. For convenience we refer to the dimensionless quantity, $\eta = hc / (\varepsilon\theta\lambda)$, and calculate opacity over $0 < \eta \leq 10.0$. Note that a black body has peak emissivity near $\eta = 3$. For each vapor the free-free optical depth, $\alpha_{ei}\Lambda$, is a function [Eqs. (A15,16)] of θ, Z, the ion density n_i, and the line average electron density N_e, as well as wave length. Note that n_i and N_e depend on Φ and Z. The quantity $\alpha_{ei}\Lambda$ includes a multiplicative Gaunt factor, of order unity, which accounts for details of the atomic physics of free-free radiation; this factor, $\bar{g}$, is a slow function of η, θ, and Z to which we have found an analytic fit [Eqs. (A17) - (A20)]. Our value of $\bar{g}$ agrees well with numerical results [Griem, Bekefi 1966] in various limits; although our $\bar{g}$ strictly applies only to hydrogenic ions we adopt its value for all species. The functional form for $\alpha_{ei}\Lambda$ is available in several references [Griem, Bekefi 1966, Bekefi 1976, Elton].

1.1.5 Optical depth from free-bound transitions of hydrogen.

The free-bound optical depth, $\alpha_{fb}\Lambda$, is proportional to $\alpha_{ei}\Lambda$, but with an additional

factor accounting for electron attachment/ionization from various bound states; see Eq. (A23,24). For a hydrogen source we consider electron binding to the first four principal quantum states, corresponding to the series limits of Lyman, Balmer, etc. radiation [Griem, Bekefi 1976]. Free-bound transitions dominate the opacity for temperatures of the order of the ionization potential.

1.1.6 Optical depth from free-bound transitions of target vapor.

We treat the multi-electron target vapor differently for $\alpha_{fb}\Lambda$, considering only electron binding to the lowest energy level, but allowing up to two charge states of the target species. The code thus computes the fraction of ions in the two adjacent charge states which bound Z; and the approximate factor [Griem, Bekefi 1976] accounting for recombination is given by Eq. (A26).

The inclusion of only one or two absorption edges in the target opacity is a simplistic approach. However, it is convenient and relatively accurate for the purposes of this initial version of the DESIRE code. We also choose to ignore line radiation in our theory, which seems to be justifiable due to the relatively small power density emitted by spectral lines, relative to the continuum radiation.

1.1.7 Electron-neutral radiation.

At low θ the vapor may be only partly ionized, and it is essential to calculate the opacity under these conditions. From the neutral atom density, $n_a = n - n_i$, the code calculates an effective electron-neutral collision frequency, ν; and the opacity $\alpha_{ea}\Lambda$ follows, Eqs. (A33) - (A36), from a knowledge of the electron density. Our model [Bekefi 1976] is based on electron collisions with neutral argon but is assumed to be roughly valid for other neutral vapor atoms.

1.1.8 Emissivity.

The total optical depth normal to the material surface is obtained for each vapor: $\alpha\Lambda = (\alpha_{ei} + \alpha_{fb} + \alpha_{ea})\Lambda$. The optical depth diametrically through each zone, for radiation through the sides of the vapor volumes, is simply $\alpha d = (d/\Lambda)\alpha\Lambda$. These factors determine to what degree surface emission is less than that of an ideal black body at the vapor's temperature, θ. The black body spectral intensity, $B(\eta,\theta)$, given by Eqs. (A39,40), is extremely large for $\theta \gtrsim 1$ eV, but, as we shall see, realistic plasma/vapors have much lower emissivity. The equation of radiative transfer [Bekefi 1966] dictates

that the intensity $I(\eta,\theta)$ of radiation emerging from a medium of uniform properties is related to the incident intensity, $I_0(\eta)$, for a given wavelength, as

$$I \;=\; B(\eta,\theta)[1 - \exp(-\alpha\Lambda)] + I_0(\eta)[\exp(-\alpha\Lambda)]$$

$$\equiv\; e(\eta,\theta) \qquad\qquad + t(\eta,\theta).$$

We refer to the first term in this expression as the emissivity; it is the radiation emitted by a medium in the absence of external illumination. Figure 3 schematically depicts the emissivity forward, backward, and sideways from the two zones' surfaces, and the four functions computed in the code are formally defined in Eqs. (A41) - (A44). Note that $e \cong B$ only for high density (e.g., solid materials) or large dimensions (e.g., stellar diameters), that is, when $\alpha\Lambda \gtrsim 1$.

1.1.9 Transmissivity.
When there is external incident radiation on a medium it will be partly absorbed before passing through. The transmissivity of each vapor is displayed in Fig. 3 and given by Eqs. (A45-46). We expect that at low densities and thicknesses, the target vapor, with $\alpha_T\Lambda_T \ll 1$, will be nearly transparent to the radiation emitted by the source. There is substantial absorption and heating of the target vapor only when N_T gets quite large.

1.1.10 Power densities.
The actual radiated power density is gotten by integrating the spectral intensity over all wavelengths. Five quantities are defined by Eqs. (A47) - (A51) and shown in Fig. 4, which represent radiated power density across surfaces: P_T (from the target vapor, towards the material surface), P_{SF} (net flux from the source vapor towards the target vapor), P_{SB} (from the source vapor, backward to the vacuum), P_{T2D} (target, sideways), and P_{S2D} (source, sideways). The particle kinetic energy input (e.g., from a plasma gun) is q_0; and $\dot{U}_4$ is the small power density input to the target from the vaporized atoms. Power loss associated with particle sinks is included with the terms $\dot{K}_s$ and $\dot{K}_T$.

1.1.11 Energy conservation.
The various power flows in Fig. 4 are integrated over time [Eqs. (A52)-(A60)] and the stored line-averaged energy

densities, U_S and U_T, are found. These quantities are needed in the next step to update the state variables.

1.1.12 Plasma state and heat capacity. The charge state Z and degree of ionization Φ are first computed at a given density n over a wide range of temperatures $(0.2 \text{ eV} \leq \theta \leq 100 \text{ eV})$. At large θ the plasmas are fully ionized and Z is inferred from a Saha model [Peterson]. In practice we find vapor shields are almost always in this high density regime, and this complicates the determination of Z, since it is a function of n, unlike in the Coronal regime. At low θ, when $Z \equiv 1$, the degree of ionization is approximated as an exponential function of θ [Brown]. The expressions for $Z(\theta)$ and $\Phi(\theta)$ are solved by iterations; see Eqs. (A67) - (A74).

At a given n and θ the heat capacity of the vapor is the sum of the particle kinetic energy (neutrals, electrons, ions) and the ionization energies invested in stripping electrons. This heat capacity, $c(\theta)$, is probably an underestimate when $z \cong 1$ and $\Phi \cong 1$, as it does not explicitly model excitation energy, but at higher and lower temperature the excitation is roughly included by making $c(\theta)$ a continuous function between discrete (integer) values of z. Figure 8 illustrates a typical function $c(\theta)$.

A table of $c(\theta)$ vs. θ is generated at each time step, and the updated θ is inferred by equating U/N to $c(\theta)$ for each vapor.

1.1.13 Surface vaporization. Using the power density, P_T, radiated from the target vapor towards the material surface, the vaporization of solid atoms is calculated. When DESIRE is used as a subroutine to A*THERMAL, the vaporization $\dot{N}_T$ is accurately given by a detailed thermodynamic treatment of the solid material. In the stand-alone version, on which the results of this report are based, we have used very simplified expressions to bypass the A*THERMAL routine. Our function $\dot{N}_T (P_T)$ is ch osen ad hoc as $\dot{N}_T = aP_T$, and the function a is found from previous runs of A*THERMAL without vapor shielding. Figure 5, as an example, includes (points) the erosion rate $(N_T/100 \text{ μs})$ for constant power densities incident on Mo for a 0.1 ms uniform pulse. Below a threshold $\left(P_T \lesssim 10 \text{ GW}/m^2\right)$ there is negligible erosion. At high heat loads

7

$\left(\gtrsim 100\,GW/m^2 \right)$ the vaporization rate, a, saturates; and the curve in the figure is the approximate $a(P_T)$ function used in our stand-alone code.

1.1.14 Observables. Code runs conclude with a calculation of the total erosion depth, δ. This depth is measurable in experiments and is the principal result of our computation. Other measurable quantities which should be compared include the spatial extent Λ of the vapors, the pressure Π, and the densities n and temperatures θ of the vapors. Likewise, the energy density, U_3, absorbed by the material surface and the energy transmission factor, $Y = U_3 / \int_0^{t_u} q_o dt$, can be found from calorimetry, and these are also known from the calculation.

2. <u>Code Validation</u>

A variety of tests were made of the important subcalculations employed in DESIRE. Theoretical constructs have been compared to more accurate atomic physics codes, and certain global results were compared to experimental measurements. In this section we briefly summarize this activity.

2.1 Opacity

Figure 6 superimposes the DESIRE-calculated optical depth (dashed) for an Al plasma on top of a detailed result [MacFarlane], assuming $\theta = 50$ eV, $n_{Al} = 6. \times 10^{26}$ m^{-3}, and $N_{Al} = 6. \times 10^{23}$ m^{-2}. An obvious difference is the appearance of multiple-line radiation in the detailed treatment. However, the line width is narrow. Furthermore, radiation transfer depends mainly on knowledge of the magnitude of continuum contributions to αL, and in this regard the calculations are in reasonable agreement. At low energies DESIRE may overestimate αL, perhaps due to the estimated input $Z = 8.4$ being too large. Note that DESIRE displays two absorption edges near 300 eV, from recombination of $Z = 8$ and $Z = 9$ components of the plasma, and this roughly agrees with the jump in αL given by the more accurate calculation. Both treatments agree that this vaporized Al foil is essentially a black body ($\alpha L \gg 1$), except in a narrow range near $hc/\lambda \cong 200$ eV.

8

2.2 Emissivity

From the opacity, the emissivity, $e(\eta)$, is calculated, and this is always less than the black body emission, $B(\eta)$. In Fig. 7 we superimpose the function $e(\eta)$ from DESIRE (open circles) on top of a detailed calculation [MacFarlane] for Al at 15 eV with $n_{Al} = 6. \times 10^{26}$ m^{-3}, and $N_{Al} = 6. \times 10^{22}$ m^{-2}. Again, except for line radiation and additional free-bound possibilities, the two results are in rough agreement. Both show that the emissivity is black at low and high energies and that it varies as $e \cong \alpha LB$, where αL is a few tenths, for 15 eV $\lesssim hc/\lambda \lesssim$ 100 eV. The DESIRE calculation assumes $Z = 3.05$ and shows absorption edges corresponding to the $Z = 3$ and 4 Lyman series limits.

2.3 Heat Capacity

An instructive calculation [Gilligan] of vapor shielding was published by Gilligan and is compared in Table II with a similar problem solved by DESIRE. Gilligan posed a problem in which a 3 eV black body photon source is incident on an Fe surface, delivering 83 GW/m^2 for a 10 μs period. At the end of 10 μs Gilligan finds $U_T/N_T = \left(0.75\,\text{MJ}/\text{m}^2\right)/\left(1.1 \times 10^{23}\,\text{m}^{-2}\right) = 43$ eV/atom; and his multi-zone vapor varies in density and temperature -- 10^{23} m$^{-3} \leq n \lesssim 10^{27}$ m^{-3} and 0.5 eV $\lesssim \theta < 3.5$ eV. He finds (ΦZ) varies from $\sim 10^{-2}$ near the surface to ~ 2 in the high temperature zones. By comparison, Fig. 8, which has the heat capacity, $c(\theta)$, for Fe at $n_T = 3. \times 10^{24}$ m^{-3}, as used in DESIRE, shows that 43 eV/atom corresponds to $\theta \cong 2.9$ eV and $(\Phi \equiv 1)\, Z \cong 2.2$. Hence our single-temperature target zone model clearly displays a heat capacity in the range of those found by Gilligan.

There are, however, also important differences between the two models in Table II. Gilligan finds $\Lambda_T = 12$ cm at 10 μs while DESIRE has only reached $\Lambda_T = 2.3$ cm, even at a much longer time. This is because Gilligan has not included any momentum input from the external power source and thus has no compression of the Fe vapor.

A more serious defect is Gilligan's calculation of large erosion, $\delta = 1.3$ μm, in only 10 μs. Experimental results [Suzuki] with ten times higher energy fluences (~ 80 GW for 100 μs) actually show $\delta \lesssim 0.5$ μm. This is because Gilligan's scenario has no source vapor to store incoming energy density.

DESIRE, in contrast, shows a power density of only 70 GW/m² to the target vapor when 157 GW/m² is incident (on the source vapor), as the source vapor stores and radiates away considerable energy.

Table II Comparison of Fe Ablation Theory

Code	MAGFIRE [Gilligan]	DESIRE
Time, μs	10.0	33.9
Heat source	3 eV black body (photons)	4 eV H plasma
Power density to source vapor, GW/m²	--	157.
Energy density to source vapor, MJ/m²	--	5.34
Power density to target vapor, GW/m²	83.	70.
Energy density to target vapor, MJ/m²	0.83	0.53
Target stored energy density, MJ/m²	0.75	0.24
Target line average density, 10^{23} m⁻²	1.10	0.97
Target heat capacity, eV/nucleus	43.	15.
Target θ_T, eV	0.5-3.5	1.7
Target density, n_T, m⁻³	10^{23} - 10^{25}	$4. \times 10^{24}$
Target Λ_T, cm	12.0	2.3
Energy density to Fe surface, MJ/m²	0.075	0.264
Surface eroded depth, δ, μm	1.3	1.14

2.4   Vapor Thickness and Plasma Pressure

More relevant tests of the DESIRE calculations lie in comparisons with directly measured experimental data. The best diagnostics of the vapor shield presently have been provided by Russian researchers and are summarized in

Table III. The table confirms the creation of rather thin target zones, $\Lambda_T \cong 0.3$ cm at 12 μs and $\Lambda_T \cong 1.0$ cm at 100 μs, with $q_0 \cong 115$ GW/m². This Λ_T is much less than Gilligans' result and more typical of DESIRE values, which include pressure balance; DESIRE predicts (Fe surface, 115 GW/m²) $\Lambda_T \cong 0.13$ cm at 12 μs and $\Lambda_T \cong 0.54$ cm at 100 μs. On MKT we note $\Lambda_s \cong 10$ cm, which also compares well with the typical value from DESIRE, $\Lambda_s \cong 11\text{-}16$ cm. The high pressures inferred by the Russian diagnostics are also in agreement with the value $\Pi \cong 3$ MPa given by DESIRE (for $E_{io} + E_{eo} \cong 30\text{-}50$ eV). Moreover, DESIRE predicts Π decreases at higher $E_{io} + E_{eo}$, which also is a trend displayed in the data.

Table III
Experimental Vapor Parameters with Hydrogen Plasma Guns
[Barabash; Strunnikov]

Plasma Gun		VIKA	MKT
Institution		Efremov	TRINITI
Pulse width, t_u	(μs)	100	~12
Heat load, q_0	(GW/m²)	40-120	~115
Spot diameter, d	(cm)	2.0	~20
Electrode/target distance, d_G	(m)	3.0	~2.0
Target material		W, Mo	Fe
E_{io}	(eV)	30-75	100-1000
E_{eo}	(eV)	-----	5-200
Λ_s	(cm)	-----	~10.
Λ_T	(cm)	≲1.0	≲0.5
θ_T	(eV)	-----	≲5
n_T	(m⁻³)	-----	≳10^{23}
Y	(%)	10	"few"
Π	(MPa)	"several"	~0.7

2.5 Vapor Temperature and Density

The MKT experiment [Strunnikov] has excellent spatial and time resolution of the parameters θ and n. These are continuous from the gun electrodes to the F_e surface; i.e., $\theta \lesssim 10^{22}$ m^{-3} at the gun and rises to n $\gtrsim 10^{24}$ m^{-3} at the surface. Within the target vapor zone (Table III) such observations agree reasonably well with typical values computed by DESIRE, $\theta_T \cong 1$ eV and $n_T \cong 5 \times 10^{24}$ m^{-3}.

2.6 Transmission Fraction and Erosion Depth

Measured values of energy transmission are seen in Table III to be Y $\lesssim$ 0.10. Additional quantitative comparisons of measured and calculated Y values will be given in Sec. 4; we generally find Y $\lesssim$ 0.05 with this present, initial version of DESIRE.

The ultimate test for DESIRE is a comparison with measured target erosion depth δ. DESIRE calculations will be compared to an extensive set of experiments [Barabash; Suzuki] and will display rather good agreement. In contrast, Gilligan's model, which neglects the energy storage and backward and sideways radiation energy loss of the source vapor, predicts [Gilligan] $\delta = 10.7$ μm at 100 μs and 8.3 MJ/m^2, which is roughly twenty-five times larger than measured for Fe [Suzuki].

3. Sample Calculation: H Gun Ablation of Mo

Here we present a detailed description of a time-dependent calculation to model an experiment with the PLADIS gun at the Univ. of New Mexico. This gun [Suzuki] was operated in hydrogen and typically produced a footprint diameter δ $\cong 2.3$ cm on the test Mo surface. The gun electrodes were positioned at $\delta_G \cong 20$ cm from the surface, but, since we calculate $\Lambda_s + \Lambda_T \lesssim d_G$, there are no particle losses for the case under study. We consider the hydrogen gun plasma to have [Gahl] $E_{io} = 30$ eV and $E_{eo} = 1$ eV, and we study a case with $q_o = 91$ GW/m^2, uniform over a time $t_u = 100$ μs. Russian studies [Strunnikov] observe the test surfaces to initially reach temperatures somewhat in excess of boiling, so we posit Mo atom vapor to be liberated at $\theta_{T_o} = 0.448$ eV.

Figure 9 shows the evolution of the source and target vapor temperatures and ionization degree. The target vapor is initially only barely ionized, as $\theta_T = 0.45$ eV is well below the first ionization potential of Mo ($X_1 = 7.1$ eV), but Φ_T

increases rapidly as θ_T rises due to the heating by the source vapor's radiation. The source vapor starts out and remains fully ionized until $t \cong 10$ µs. During this first phase the hydrogen radiates inefficiently, but as θ_S eventually drops to ~6 eV the recombination radiation absorption edges arise, leading to a spike in the hydrogen radiated power. As a consequence of this power loss the source temperature abruptly collapses. Beyond $t \cong 30$ µs the hydrogen radiative loss diminishes; and both source and target vapors are only partially ionized, with slowly dropping temperatures.

Figure 10 displays the energy density and power radiated by the source vapor. Initially the number density N_S is so small that the source is optically thin and the radiated power is small, being much less than the input power, $q_0 = 91$ GW/m^2. The energy density U_S consequently increases. At the time of radiative collapse the power densities spike and U_S drops. The backward radiation is not shown, but $P_{SB} \cong P_{SF}$. The sideways radiated power density, P_{S2D} is less than P_{SF}, however near the end of the pulse the source zone thickness, Λ_s, is so large that the power radiated out the sides is the dominant energy sink. Reference to Fig. 11 shows that the target vapor radiates towards the solid surface with $P_T \cong P_{SF}$. Recall that Mo has a threshold of ~10 GW/m^2 to suffer vaporization (Fig. 5); this explains the target vapor production (N_T) in the figure, which occurs when $t \cong 15$ µs. The target's sideways radiated power density is small, $P_{T2D} < P_T$, since P_{T2D} arises from Mo vapor emission at a relatively low temperature $\left(\theta_T^4 < \theta_s^4\right)$, while P_T is predominantly radiation transmission through the target zone.

Figure 12-14 show the optical thickness and spectral intensities of both vapors at $t = 13$ µs. The Lyman and Balmer absorption edges are prominent for the hydrogen source at ~6 eV (during the radiative collapse). The effect of this free-bound radiative opacity is the two peaks in the source emissivity, e_S, near $\eta_S = 0.6$ and 2.3 in Fig. 13. Note, however, $\alpha_S \Lambda_S << 1$ so $e_S(\eta)$ is quite small compared to black body emissivity. The target vapor at 1 eV exhibits the absorption edge of Mo$^+$ recombination into the Mo ground state; the corresponding wavelength of 0.17 µm is at $\eta_S = 1.1$ for a source temperature $\theta_S = 6.1$ eV. A comparison of Figs. 14 and 13 shows the weak absorption of the

target vapor, $\alpha_T \Lambda_T \lesssim 1$, with the target transmissivity nearly equal to the source emissivity.

Despite the transparency of the target vapor, relatively little of the plasma gun energy arrives at the Mo surface; the fraction is only $Y = 0.45$ MJ/9.1 MJ = 0.049. Most of the incident energy is radiated by the source vapor sideways ($U_3/U_1 = 6.8$ MJ/9.1 MJ) and backward ($U_2/U_1 = 0.55$ MJ/9.1 MJ). At the end of the pulse the source vapor also stores considerable energy density due to its heat capacity ($U_s/U_1 = 1.2$ MJ/9.1 MJ). The target vapor stores relatively little energy density and losses little to sideways radiation. Due to these sundry heat sinks the vapor shielding is quite effective, the ablation depth being only $\delta = 0.29$ μm for Mo with $\rho = 9000$ kg/m^3.

4. DESIRE Code Comparison with Plasma Gun Data

Code validation is best achieved by comparison with experiments, which we have done for various metal surfaces and different plasma gun conditions. For these tests we ran DESIRE in the stand-alone mode, using unshielded vaporization models (as in Fig. 5) generated from previous A*THERMAL runs. The calculations assume a sine-shaped wave form for the heat load, of total length 100 μs.

Figure 15, adapted from [Suzuki], shows three data points of measured energy transmission fraction to a tungsten calorimeter through the vapor clouds generated under specified heat loads. The gun energy density, noted by the abscissa, was determined from discharges into a deep copper bucket calorimeter, which accounted for total plasma energy, including sideways-radiated losses. When the DESIRE code is run with a fixed initial ion kinetic energy from the plasma gun, $E_{io} = 30$ eV, the calculation shows Y decreasing as U_1 increases from 6 MJ/m^2 to 16 MJ/m^2. Yet the data suggest Y increases with U_1; so we conclude that E_{io} may be increasing with U_1. (This is not unreasonable, as, for a fixed pulse width, e.g., 100 μs, the experimental set-up keeps the bank capacitance constant and increases U_1 by raising the voltage on the bank.) Whereas $E_{io} \cong 30$ eV agrees with the data at $U_1 = 6$ MJ/m^2, apparently $E_{io} \gtrsim 100$ eV would be needed to duplicate the data at 16 MJ/m^2.

14

Target erosion is an obvious test for DESIRE. The experimental data (points) in Fig. 16 [Suzuki] display the average ablation depth of steel found at four different values of U_1. There is a wide, inconsistent scatter of results with only slight differences in target composition, so we cannot expect DESIRE to fully explain the observed erosion. However, it is evident, in the experiment and from the DESIRE results for pure Fe, that minimal erosion occurs below $U_1 \cong 5$ MJ/m^2. Yet substantial erosion occurs for $U_1 \gtrsim 10$ MJ/m^2. The code results show this onset of erosion is associated with an ablation threshold, such as is illustrated in Fig. 5 for a similar metal surface. Note also that the DESIRE curve at $E_{io} = 30$ eV is in good agreement with the data at $U_1 \lesssim 12$ MJ/m^2, while it underestimates erosion at 16 MJ/m^2. This is additional evidence suggesting the plasma gun produces higher ion kinetic energies at large U_1.

The agreement of the DESIRE model with the experiment, shown in Fig. 16, is much better than the MAGFIRE result [Gilligan] which found $\delta = 10.7$ μm at $U_1 = 8.3$ MJ/m^2. This emphasizes the importance of the additional heat sinks incorporated in our treatment.

Molybdenum targets were tested with both U.S. and Russian plasma guns, and the experimental data, in Fig. 17, again show [Gahl; Barabash] how typically there is a scatter of results under similar conditions. The horizontal error bars from VIKA are a measure of uncertainty in the energy content delivered in the plasma pulse, and the vertical scatter of PLADIS points indicate a certain lack of reproducibility in these experiments. Some difference between the two institutional results may be attributed to subtle geometric differences; for example, VIKA had $d_G = 3.0$ m but PLADIS had gun electrodes much closer to the target. The DESIRE results shown treated both geometries the same. Our calculated erosion with $E_{io} \cong 30$ eV - 50 eV is in approximate agreement with the data. Time-of-flight measurements on PLADIS suggest the leading edge of the gun pulse is populated by protons at a few tens of electron volts [Gahl], which is perhaps a bit lower than $E_{io} \cong 30$ eV - 75 eV reported on VIKA (see Table III).

Erosion of tungsten was likewise measured on both VIKA and PLADIS, and the results are shown in Fig. 18 along with the DESIRE calculations. In the experiments tungsten appears more robust than Mo under the same heat pulse conditions.

Both experiment [Gahl] and the DESIRE theoretical model show beryllium to suffer more erosion than the three metals discussed above, which is evident from Fig. 19. A noteworthy point illustrated in the graph is that the central depth of the damage crater is roughly triple the average depth, as inferred from mass loss measurements. The nonuniform crater depth may be associated with a depression in the melt layer, possible redeposition or splashing of the melt toward the edges, and nonuniform heat deposition by the gun plasma. Such details are not included in the present DESIRE model.

5. Conclusions

Although our atomic physics models are very simplified we are able to duplicate many observed features of plasma gun ablation experiments with a reasonable accuracy.

The constraints and caveats on our approach are legion and can be enumerated:

1. normal incidence on target assumed
2. no loss of melt layer
3. no redeposition of vapor
4. single element (non-alloy) metal target
5. two vapor zones with homogeneous properties
6. no mixing between zones
7. no thermal conduction through vapors
8. no heat convection or Rayleigh-Taylor instability of zones
9. line radiation is ignored
10. instantaneous pressure balance between zones (no free expansion of vapor)
11. no loss of neutral pressure upon vapor cooling
12. no reflected radiation from any surface
13. no model for two dimensional profile of crater depth
14. gun electrodes presently assumed far from target ($d_G \gg 100$ cm)
15. pure hydrogen plasma source with $E_{eo} + E_{io} \lesssim 50$ eV.

16

On first glance it might appear that the omission of so many physics details would constitute an egregious shortcoming for our model. Nevertheless, the DESIRE routine is evidently quite successful for studying plasma gun ablation, and the last caveat in the list is the principal issue needing further work. We hope, in fact, that by extending the code capability to $E_{io} \gtrsim 100$ eV we will be better able to duplicate the experimental data, such as shown in Figs. 15 and 19.

Acknowledgments

References

Barabash, V.R., et al., Fusion Eng. and Design 18 (1991) 145.

Bekefi, G., Radiation Processes in Plasmas (Wiley, New York, 1966).

Bekefi, G., et al., in Principles of Laser Plasmas, G. Bekefi, ed. (Wiley, New York, 1976).

Brown, S.C., Introduction to Electrical Discharges in Gases (Wiley, New York, 1966).

Elton, R.C., in Methods of Experimental Physics, Vol. 9, Part A, H.R. Griem and R.H. Loverg, eds., (Academic Press, New York, 1970).

Gahl, J.M., private communication.

Gilligan, J., et al., J. Nucl. Materials 162-164 (1989) 957.

Griem, H.R., Plasma Spectroscopy (McGraw-Hill, New York, 1964).

Hassanein, A., J. Nuc. Materials 122/123 (1984) 1453.

MacFarlane, J.J., Wang, P., Lasers and Particle Beams 10 (1992) 349.

Peterson, R.R., Moses, G.A., Comput. Phys. Commun. 28 (1983) 405.

Strunnikov, V.M., private communication.
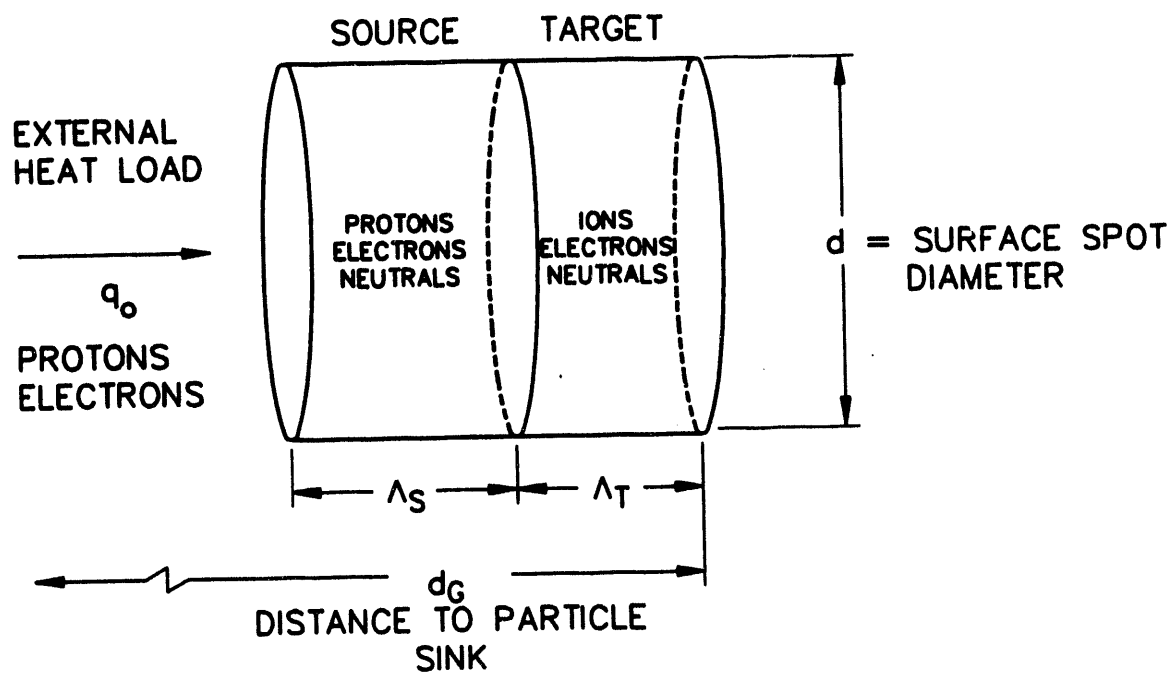
Suzuki, S., et al., J. Nucl. Materials 200 (1993) 265.
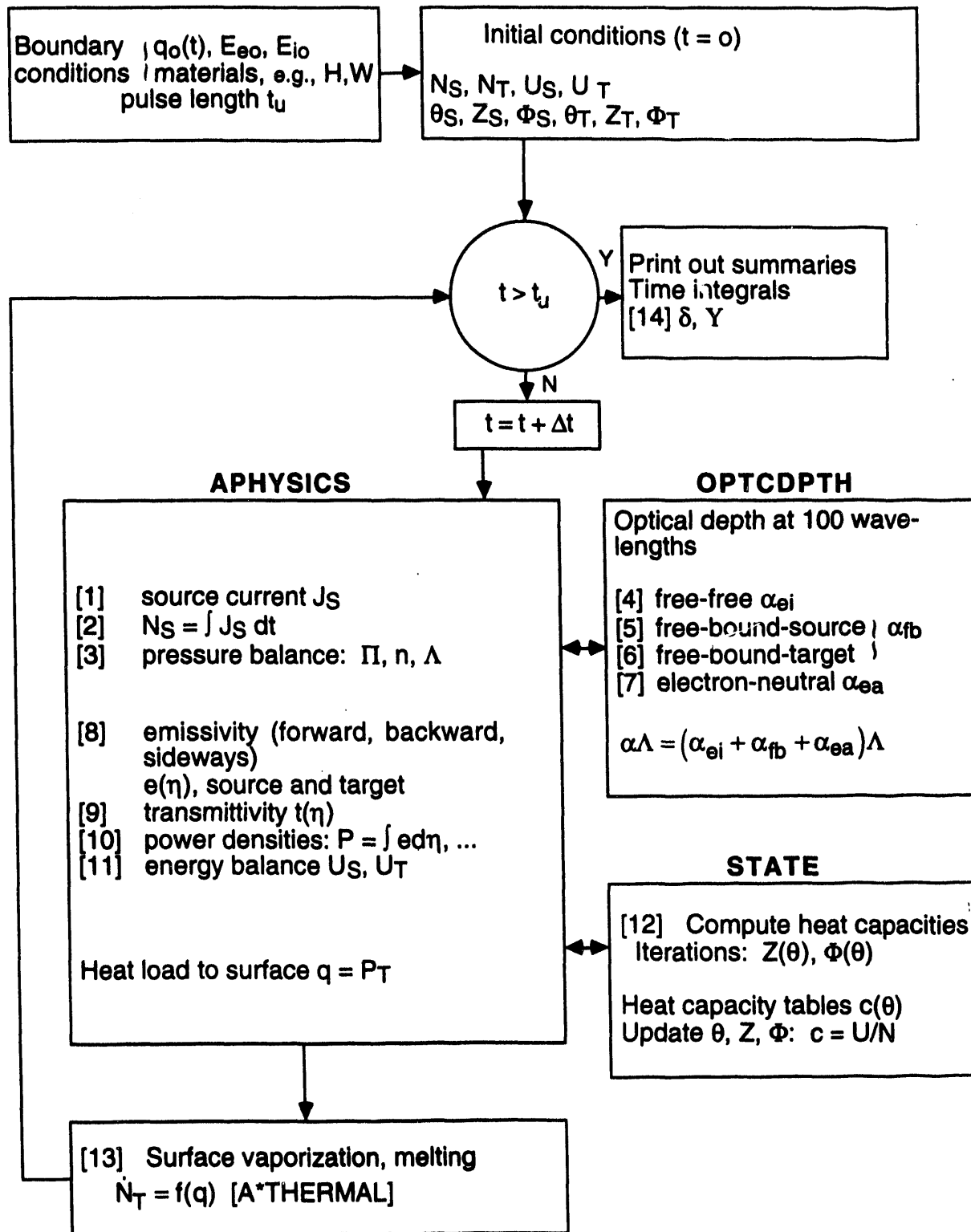
Figure 1. Geometry, cylindrical footprint.

Figure 2. DESIRE flowchart.

Boundary conditions $\{ q_0(t), E_{eo}, E_{io}$ materials, e.g., H,W pulse length t_u

Initial conditions (t = o)

N_S, N_T, U_S, U_T
θ_S, Z_S, Φ_S, θ_T, Z_T, Φ_T

$t > t_u$

Y | Print out summaries
Time integrals
[14] δ, Y

N

$t = t + \Delta t$

APHYSICS

[1] source current J_S
[2] $N_S = \int J_S$ dt
[3] pressure balance: Π, n, Λ

[8] emissivity (forward, backward, sideways)
e(η), source and target
[9] transmittivity t(η)
[10] power densities: $P = \int e d\eta$, ...
[11] energy balance U_S, U_T

Heat load to surface q = P_T

OPTCDPTH

Optical depth at 100 wave-lengths

[4] free-free α_{ei}
[5] free-bound-source $\}$ α_{fb}
[6] free-bound-target $\}$
[7] electron-neutral α_{ea}

$\alpha\Lambda = (\alpha_{ei} + \alpha_{fb} + \alpha_{ea})\Lambda$

STATE

[12] Compute heat capacities
Iterations: Z(θ), Φ(θ)

Heat capacity tables c(θ)
Update θ, Z, Φ: c = U/N

[13] Surface vaporization, melting
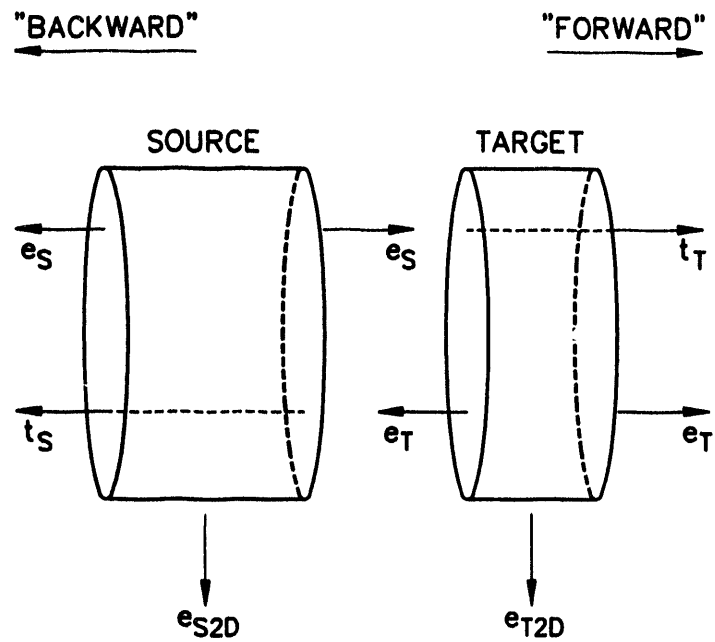$\dot{N}_T = f(q)$ [A*THERMAL]

19

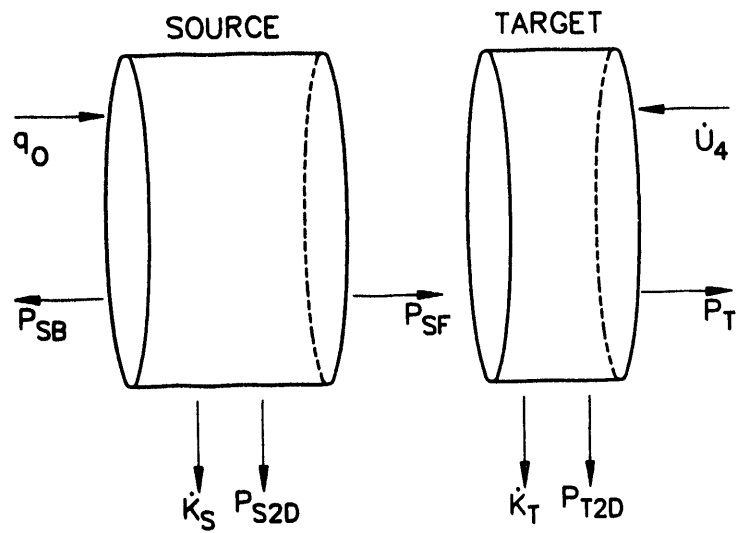Figure 3. Power flow -- spec ral intensities.
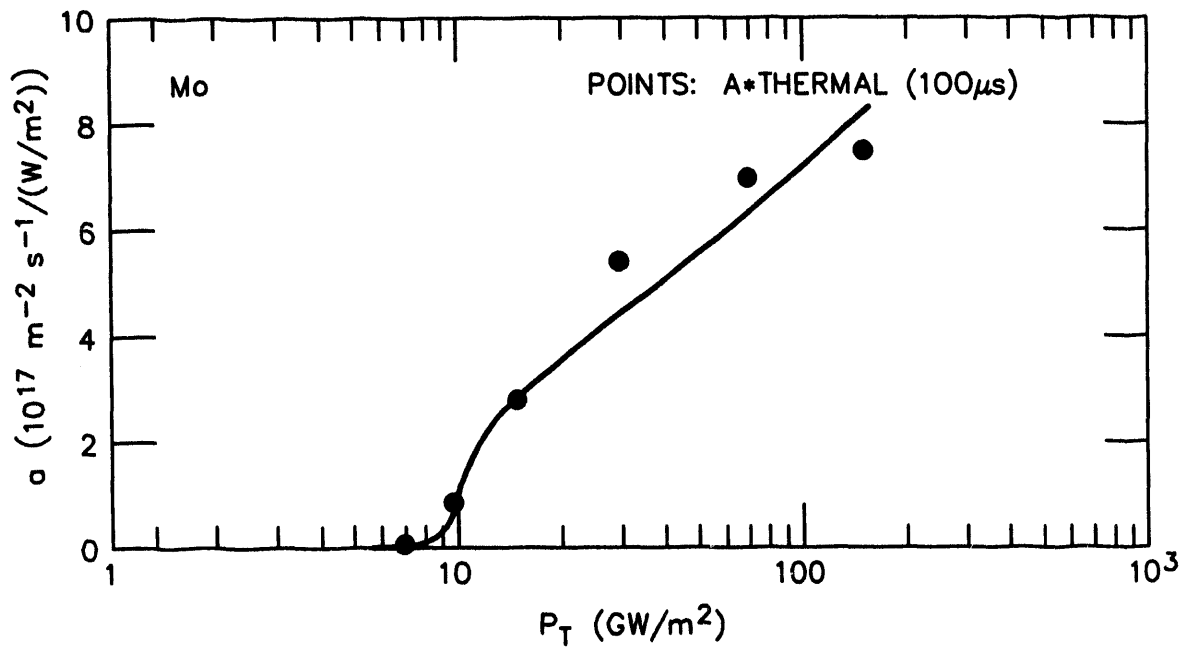
Figure 4. Power flow -- radiation and particles.
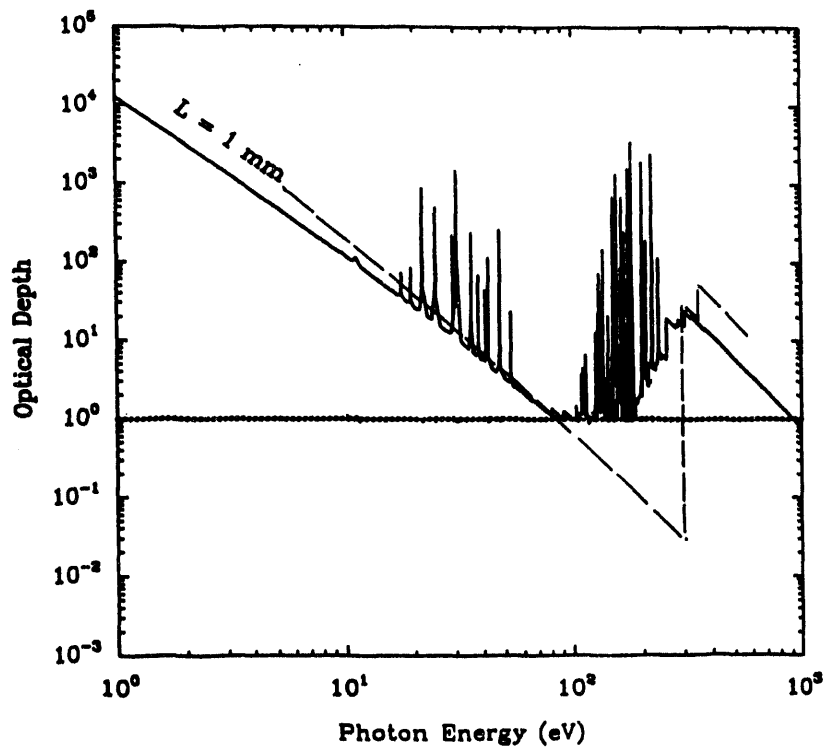
Figure 5. Evaporation of unshielded surface (Mo).

Figure 6. Optical depth vs. photon energy: Al at 50 eV and 6×10^{26} m^{-3}, Z=8.4, with a thickness L = 1.0 mm. Solid curve from MacFarlane and Wang; dashed from DESIRE.
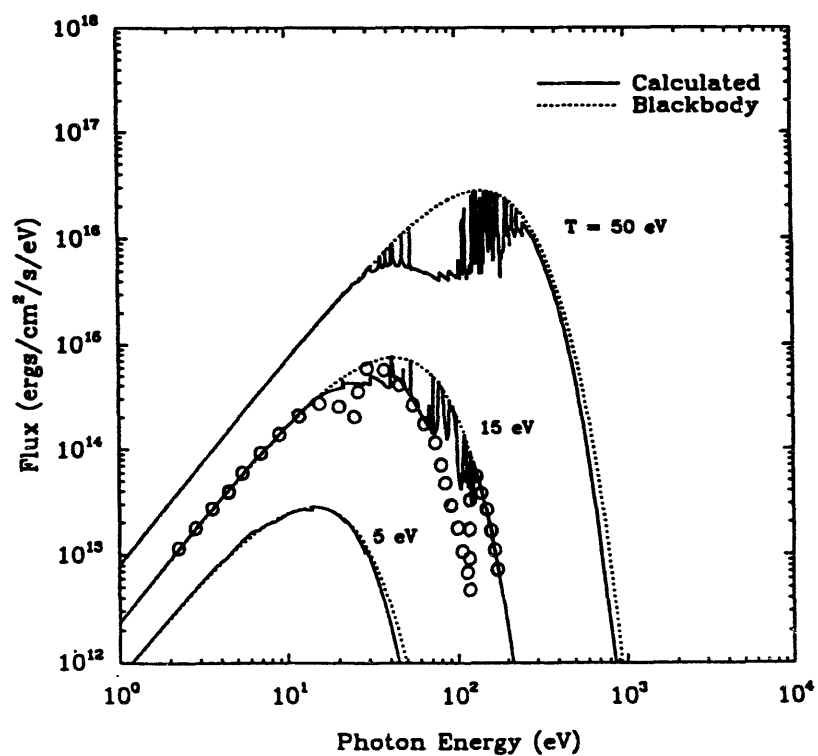
Figure 7. Emissivity of Al plasma at 6×10^{26} m^{-3} and L=0.1 mm. Dotted curves are black body; solid curves from MacFarlane and Wang; open circles from DESIRE for θ = 15 eV.
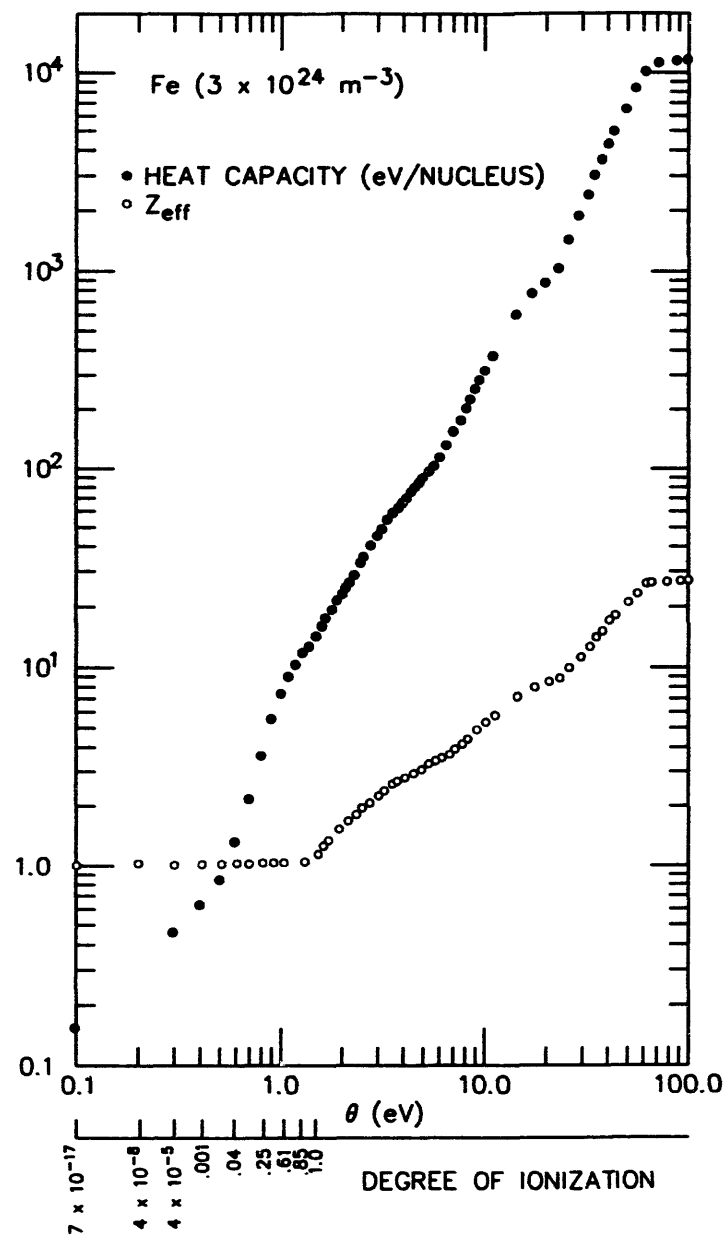
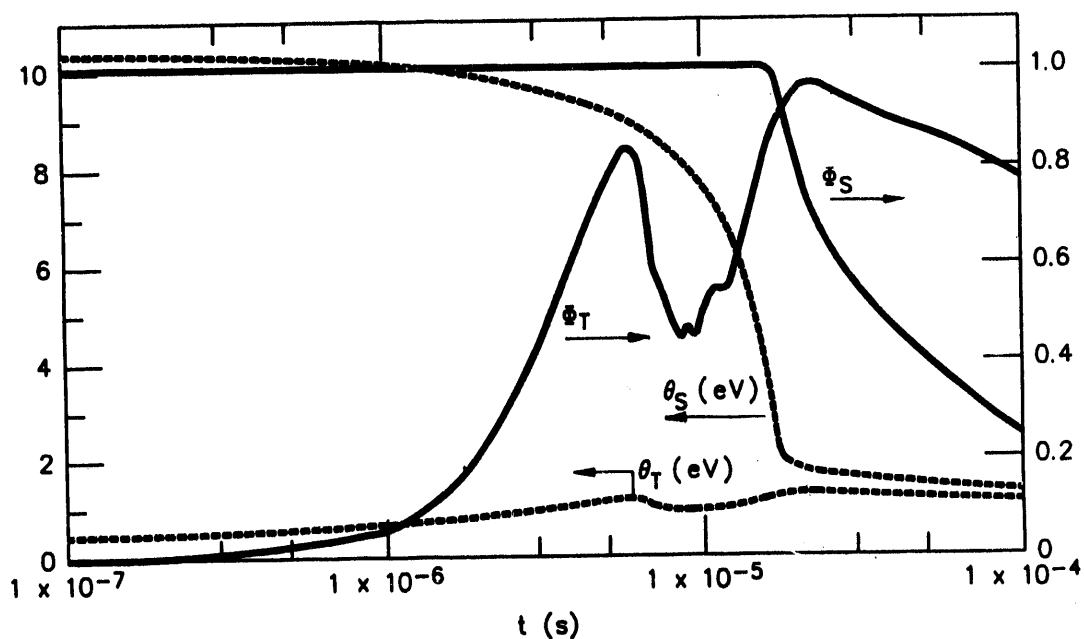Figure 8. Heat capacity and charge state for iron.

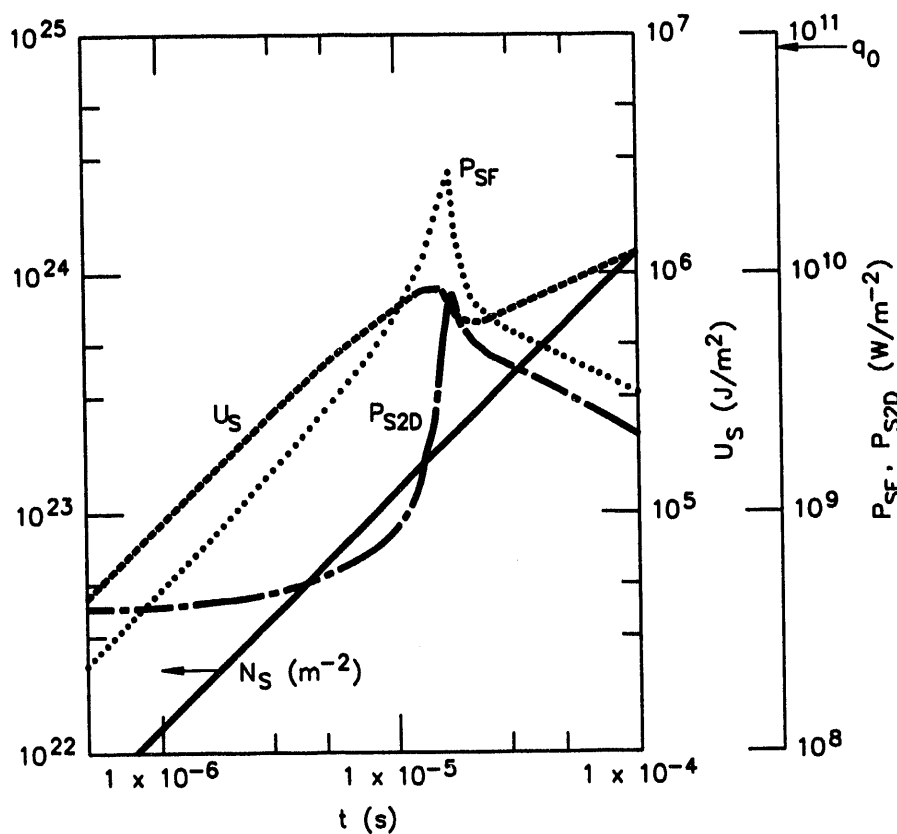Figure 9. Source and target vapor temperatures and ionization degree.

Figure 10. Source vapor: number density, energy density, radiated power.

23
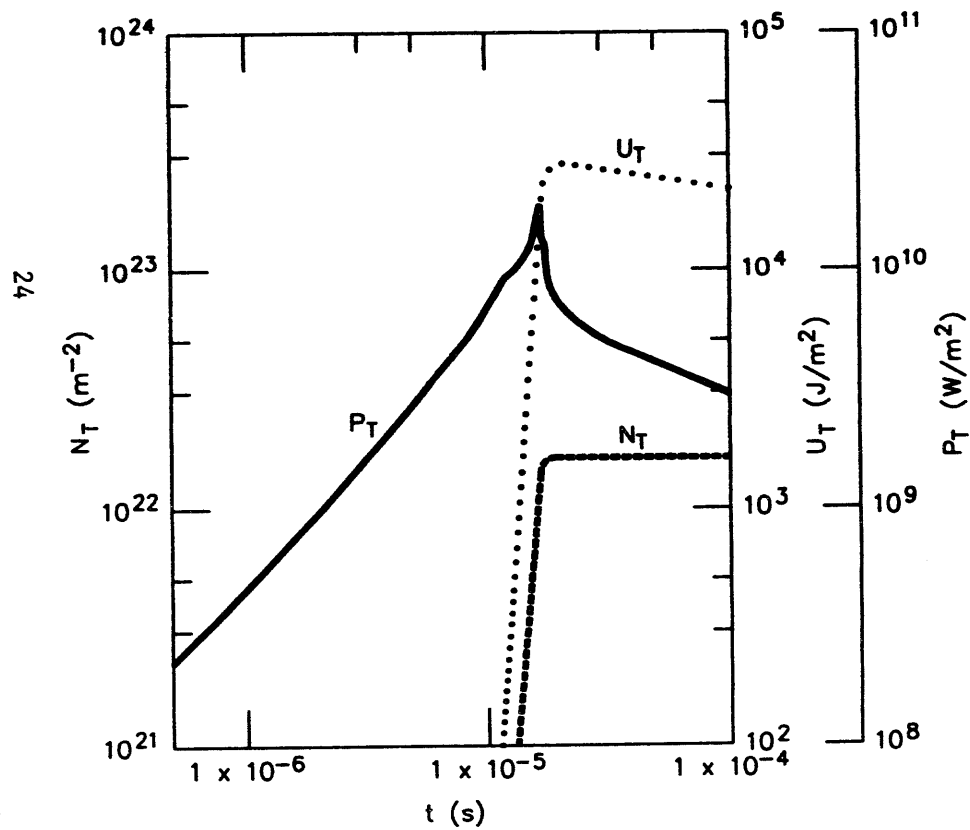
Figure 11. Target vapor: number density, energy density, power radiated to material surface.
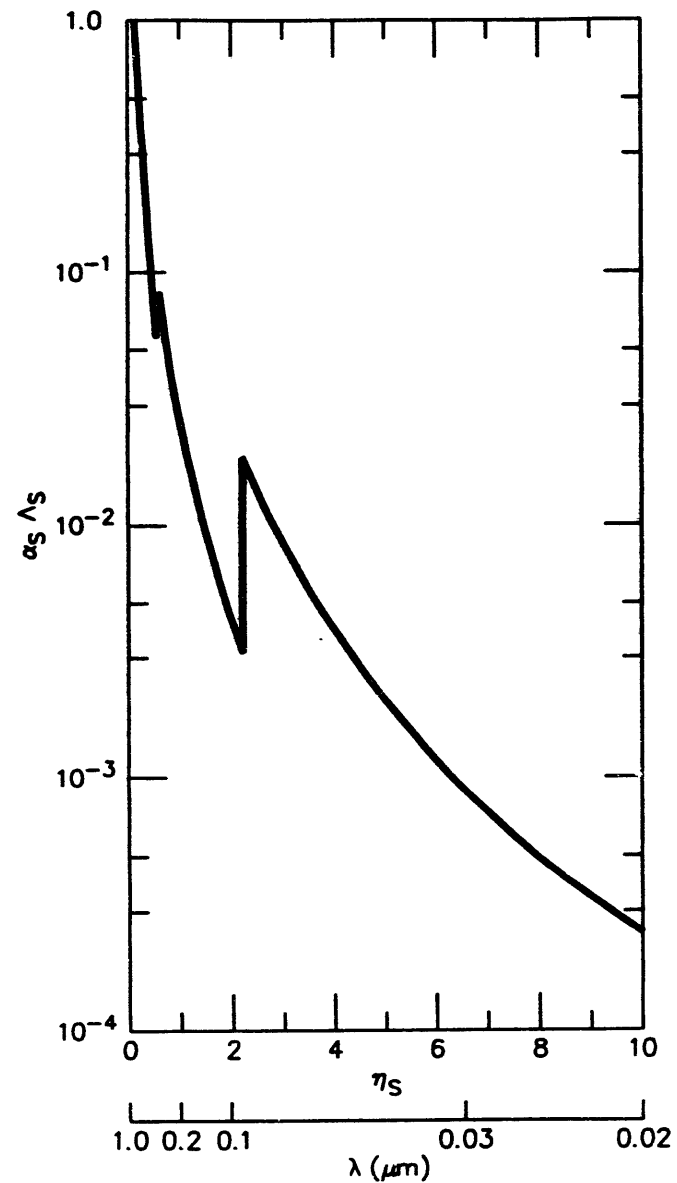
Figure 12. Opacity of H (6.1 eV, 8.2×10^{23} m^{-3}, Λ_S 20 cm).
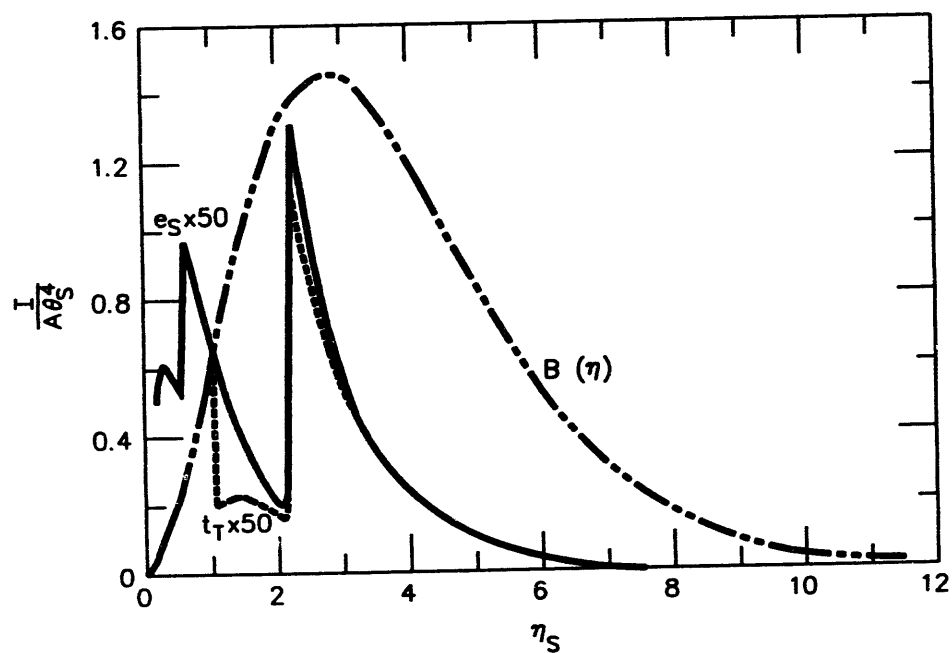
Figure 13. Spectral intensities: black body emissivity at 6.1 eV, hydrogen source emission at 6.1 eV, Mo target vapor transmissivity at 1.0 eV.
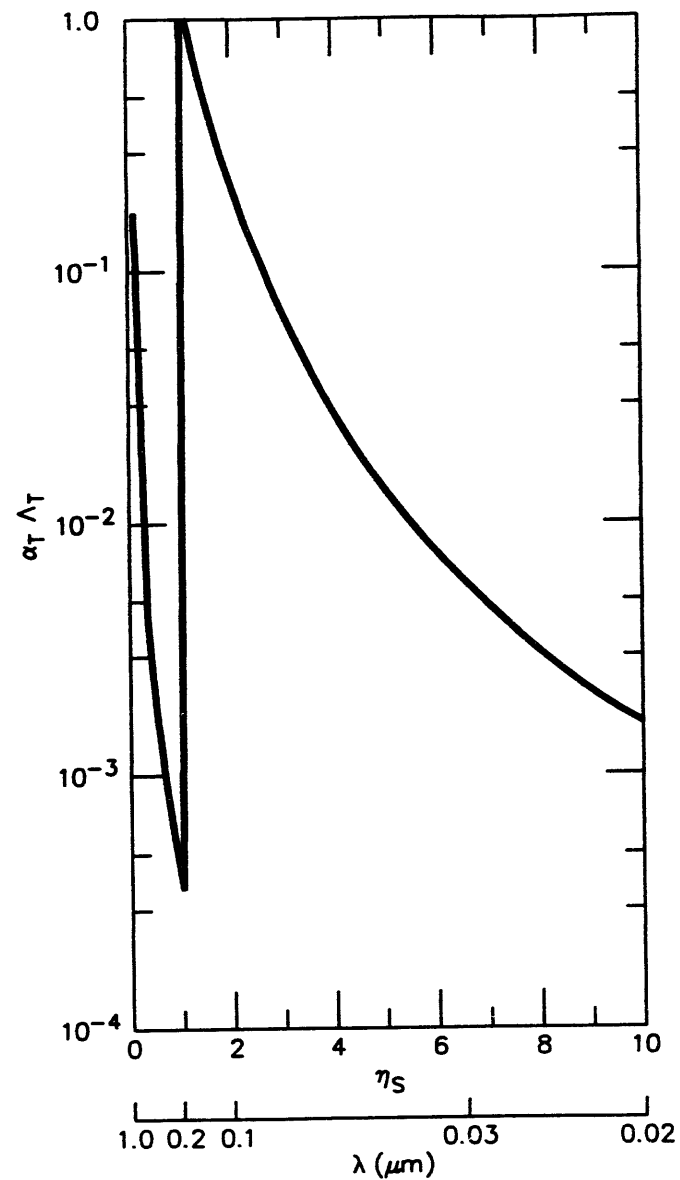
Figure 14. Opacity of Mo (1.0 eV, $6.\times10^{24}$ m^{-3}, $\Lambda_T = 0.14$ mm).
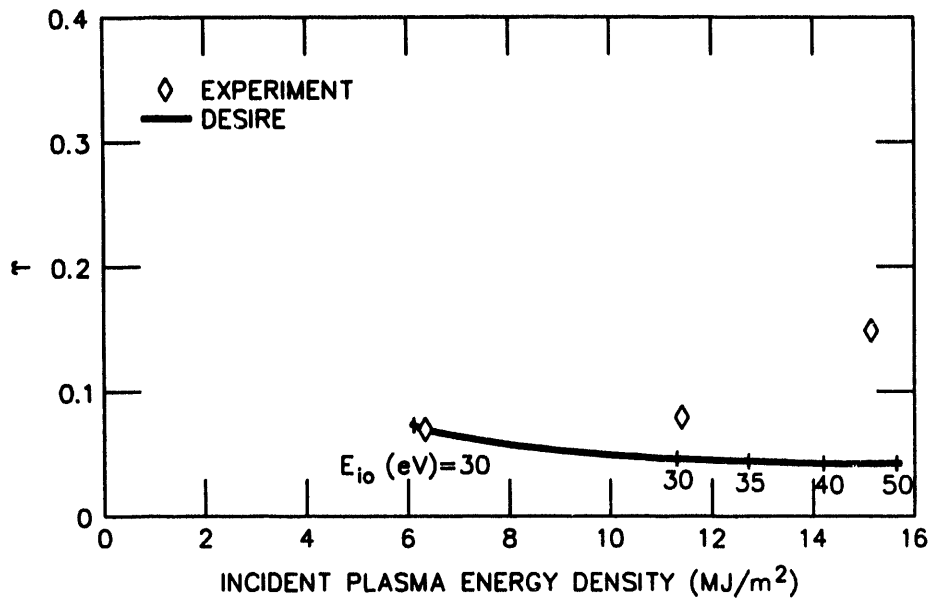
Figure 15. Energy transmission fraction to W calorimeter (t_u = 100 µs) from H plasma gun.
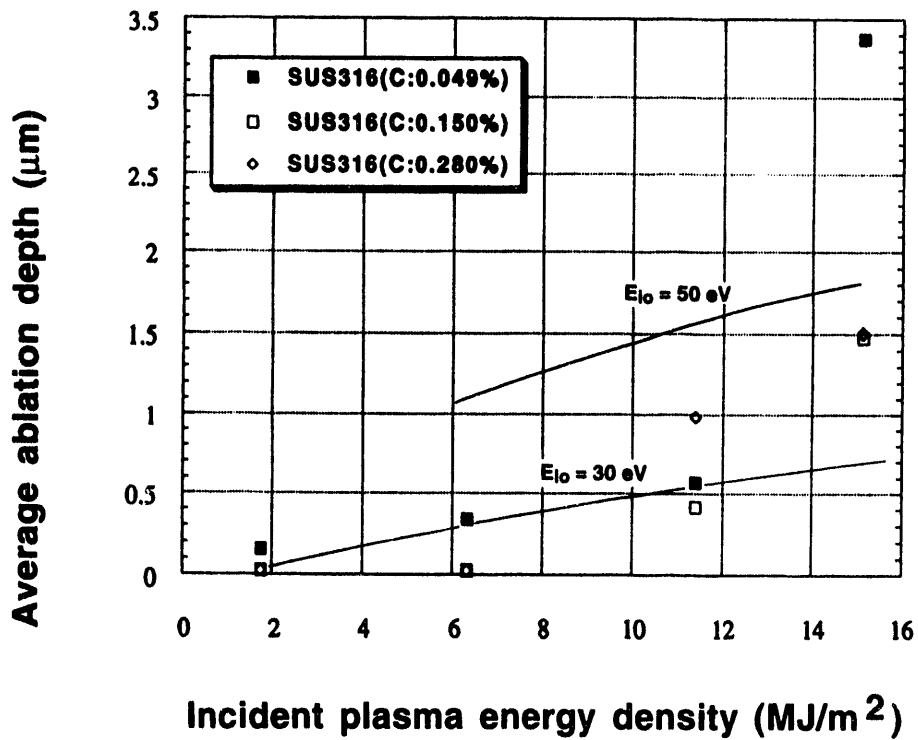
Figure 16. Ablation of Fe (t_u = 100 µs) by H plasma gun.

Figure 17. Ablation of Mo (t_u = 100 µs) by H plasma guns.

Figure 18. Ablation of W (100 µs) by H plasma guns.
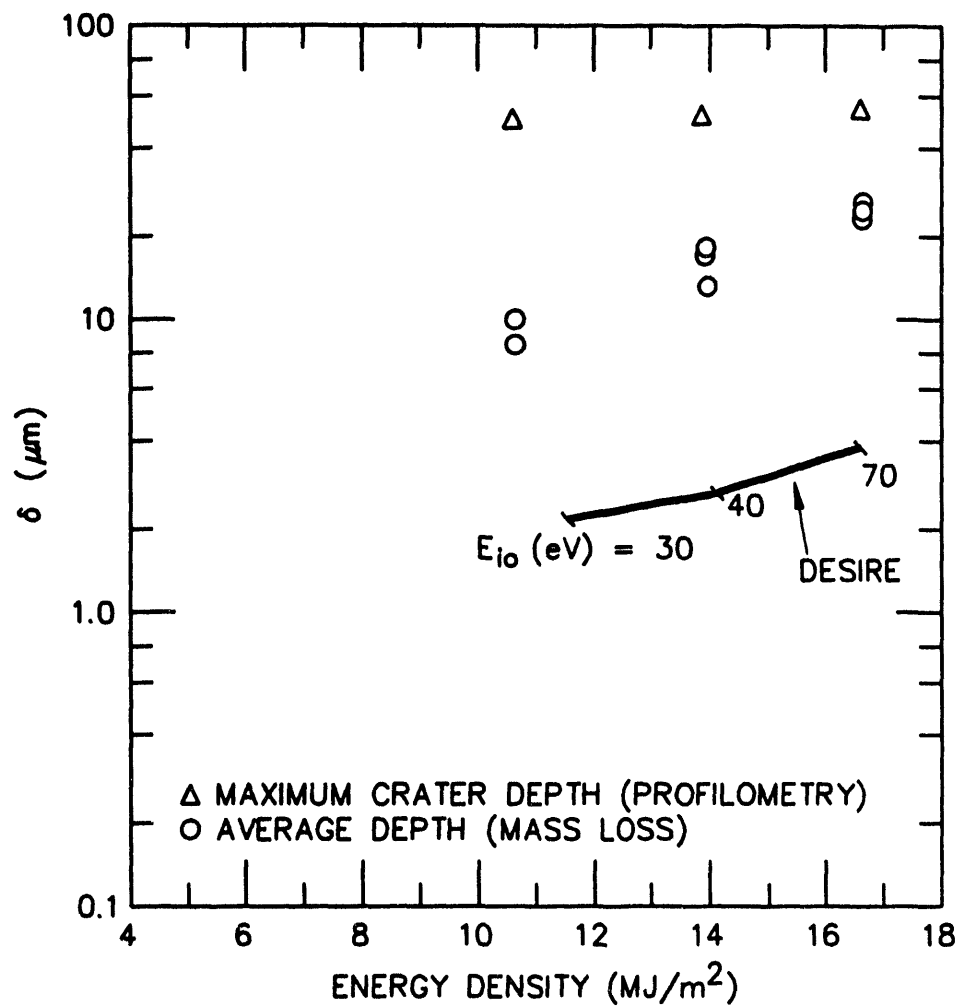
Figure 19. Ablation of Be (100 μs) by H plasma gun.

28

APPENDIX: VAPOR SHIELDING EQUATIONS

The DESIRE code uses SI units, except temperature, ionization potentials, and particle kinetic energies are in eV.

Known quantities are the boundary conditions: q_o (power density input to the source vapor), E_{eo} and E_{io} (electron and ion kinetic energy entering the source vap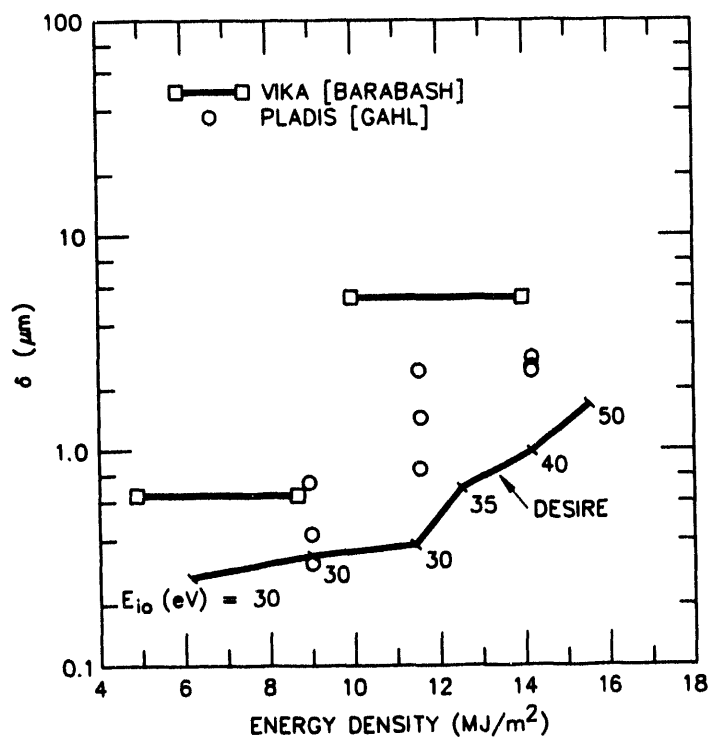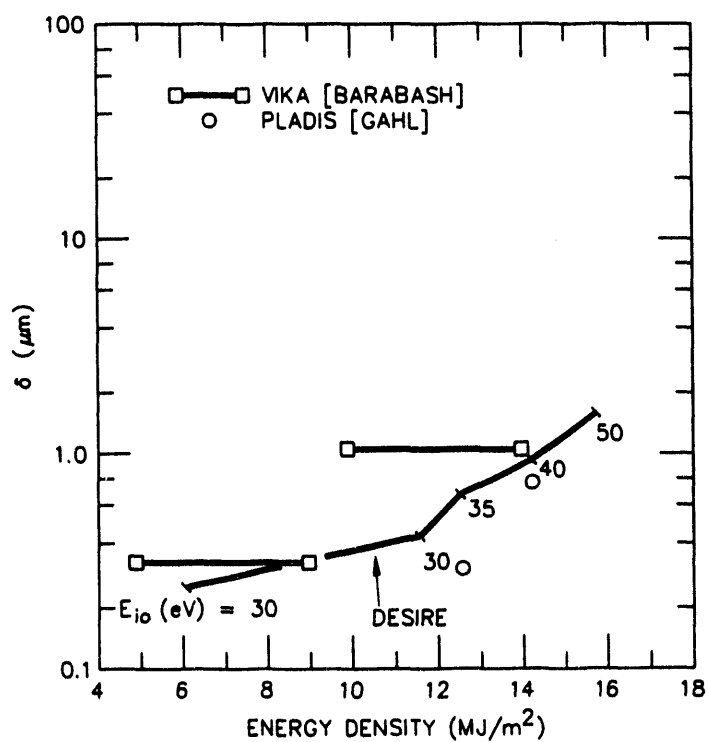or); and θ_{To} (temperature of vaporized atoms boiled off surface) and ρ (atom number density of solid surface). Geometry inputs are d (diameter of source footprint on surface) and d_G (distance from surface to particle sink, such as plasma gun electrodes). In addition to θ_{To}, information relating the target vaporization rate to the power density on the surface, $\dot{N}_T = f(P_t)$, must be known (e.g., as given by a code such as A*THERMAL). Constants in these calculations are: c (speed of light), h (Planck's constant), and χ_H (ground state ionization potential of hydrogen).

The equations displayed are specialized to the case of a hydrogen plasma source. The subscripts S and T refer respectively to the source and target vapor species.

The current density (of protons) of the fully ionized external source, J_S, is related to the incoming power density

$$q_o = \varepsilon \, J_s \left(E_{eo} + E_{io} + \chi_H \right) \tag{A1}$$

where $\varepsilon \equiv 1.602 \times 10^{-19}$ J/eV. The line average source vapor density (protons plus neutral hydrogen), N_S, is the time-integrated external current density minus particle losses

$$N_S = \int_0^t J_S \, dt - \int_0^t \dot{L}_S \, dt. \tag{A2}$$

The speed of the incoming ions is

$$v_s = \sqrt{2 \, \varepsilon \, E_{io} / m_S} \tag{A3}$$

where m_S is the proton mass. Assuming the externally supplied ions have a velocity nearly normal to the target surface, their momentum input provides an impulse which sustains a pressure

$$\Pi = J_S \, m_S \, v_S. \tag{A4}$$

We assume an instantaneous pressure balance, such that the source vapor's pressure is

$$n_S \, \varepsilon \, \theta_S \left(1 + \Phi_S \, Z_S\right) = \Pi, \tag{A5}$$

where n_S, θ_S, Φ_S, and Z_S are respectively the source vapor density, temperature, degree of ionization and charge state. The first term on the l.h.s. is due to ions and neutral atoms, and the second is due to electrons. The target vapor is likewise in pressure balance, so

$$n_T \, \varepsilon \, \theta_T \left(1 + \Phi_T \, Z_T\right) = \Pi. \tag{A6}$$

For our model of homogeneous, uniform density and temperature within each zone, the source and target vapor thicknesses, Λ_S and Λ_T, are simply given by

$$n_S = N_S \, / \, \Lambda_S \tag{A7}$$

$$n_T = N_T \, / \, \Lambda_T. \tag{A8}$$

For each vapor the optical depth is calculated as a function of wavelength, λ, although we explicitly refer to intermediate dimensionless variables,

$$\eta_S = hc/(\varepsilon\theta_s\lambda) \text{ and } \eta_T = hc/(\varepsilon\theta_T\lambda),$$

which represent the photon energy normalized to the plasma temperature. (In what follows we present formulas for the source vapor, and it is understood that analogous equations are used for the target vapor.) For opacity calculations the following quantities are needed:

the electron line average density $N_{eS} = \Phi_S Z_S N_S$,   (A9,10)

the ion density $n_{iS} = \Phi_S n_S$,   (A11,12)

and the neutral density $n_{aS} = (1 - \Phi_S)n_S$.   (A13,14)

In our model we calculate only continuum radiation and include three contributions to the opacity. First, free-free (electron-ion Bremsstrahlung) radiation results in an optical depth

$$\alpha_{eiS} \Lambda_S = \frac{3.09 \times 10^{-17} N_{eS} n_{iS} Z_S^2 \left[1 - e^{-\eta_s}\right]\left\{\pi \bar{g}_S / \sqrt{3}\right\}}{\omega^2 \theta_S^{1.5} \eta_s}, \quad (A15,16)$$

where $\omega = 2\pi c/\lambda$. The free-free Gaunt factor, $\bar{g}_S$, of order unity, is a function of λ, θ_S, and Z_S. We developed the following simple fit to calculated $\bar{g}_S$ values over a wide range:

$$\bar{g}_S = \tilde{g}_S (\eta_S)\left[1 + 0.7364 \sqrt{\eta_S} \exp(-0.06415 \tau_S)\right] \quad (A17,18)$$

where

$$\tilde{g}_S = \begin{cases} \left(\sqrt{3}/\pi\right) \exp(\eta_S/2) \, \ell n(2/\eta_S), & \eta_S < 0.4 \\ 1.08379 - 0.25937 (\eta_S - 0.4), & 0.4 \leq \eta_S < 1.6 \\ \sqrt{3/(\pi \eta_S)}, & 1.6 \leq \eta_S \end{cases} \quad (A19,20)$$

and

$$\tau_S = \theta_S / \left(Z_S^2 \chi_H\right). \quad (A21,22)$$

At small η we impose the constraint that $\bar{g} \leq 10$.

31

The free-bound optical depth (from recombination, photo-ionization processes), $\alpha_{fbS} \Lambda_S$, is proportional to the free-free contribution, with

$$\alpha_{fbS} = \alpha_{eiS} \left(\frac{2 \chi_H}{z_S^2 \theta_S} \right) G(\bar{g}_S) F_S. \qquad (A23,24)$$

We approximate free-bound Gaunt factors with the function

$$G(\bar{g}) = \begin{cases} 1 & , \ \bar{g} \le 0.95 \\ 0.95/\bar{g}, & 0.95 < \bar{g} \end{cases}.$$

The function F is a sum over possible recombination processes and our model treats a hydrogen source differently from the target vapor.

For a hydrogen source vapor we sum over recombination into four principal quantum number states:

$$F_S \quad = H(\omega_1) \exp[\chi_H/\theta_S] + 0.5\,H(\omega_2) \exp[\chi_H/(4\theta_S]$$

$$+ 0.14815\,H(\omega_3) \exp[\chi_H/(9\theta_S)] + 0.14063\,H(\omega_4) \exp[\chi_H/(16\theta_S)], \quad (A25)$$

where $H(\omega_n)$ is the step function

$$H(\omega_n) = \begin{cases} 0, & \omega < \omega_n \\ 1, & \omega_n \le \omega \end{cases}.$$

The four absorption edges occur at $h\omega_n/2\pi = \varepsilon \chi_H/n^2$, $n = 1, 2, 3, 4$, which represent the (n=1) Lyman series limit at $\omega_1 = 2.06 \times 10^{16}$ s^{-1} ($\lambda_1 = 0.09137$ μm), the (n=2) Balmer limit ($\lambda_2 = 0.3655$ μm), etc.

For the target vapor we consider only ground state (n=1) recombination for two ionization states:

$$F_T = \sum_{j=\ell}^{\ell+1} \frac{n_j}{n_i} \frac{j^4}{Q_j^3} \exp\left(\chi_j/\theta_T\right) H(\omega_j), \qquad (A26)$$

in which the effective quantum number is $Q_j = j\sqrt{\chi_H/\chi_j}$. In our notation χ_j represents the jth ionization potential of the target species, and $\hbar\omega_j/2\pi = \varepsilon\chi_j$. The two terms in F_T are weighted by the relative density of the two adjacent ionization states which bracket the effective charge of the target plasma. We use a simple linear combination of densities, i.e.,

$$\begin{cases} Z_T = \dfrac{n_\ell}{n_i}[[Z_T]] + \dfrac{n_{\ell+1}}{n_i}[[Z_T + 1]] & \text{(A27)} \\[4mm] 1 = (n_\ell/n_i) + (n_{\ell+1}/n_i), & \text{(A28)} \end{cases}$$

where $[[Y]]$ denotes the next integer smaller than Y. For a partially ionized target vapor ($\Phi_T < 1$) or for fully stripped ions ($Z=Z_{Max}$) only one term is retained in F_T, with $n_\ell/n_i = 1$.

The third contribution to the optical depth is from electron-atom collisions. The partial pressure of neutral atoms is

$$\Pi_{aS} = n_{aS}\varepsilon\theta_S, \tag{A29,30}$$

and this results in an effective electron-neutral collision frequency

$$\nu_S = \begin{cases} 2.78 \times 10^5\,\Pi_{aS} & , \ \theta_S < 0.1\,\text{eV} \\[2mm] 9.751 \times 10^6\,\Pi_{aS}\,\theta_S^{1.545} & , \ 0.1\,\text{eV} \le \theta_S \le 3.0\,\text{eV} \\[2mm] 5.323 \times 10^7\,\Pi_{aS} & , \ 3.0\,\text{eV} \le \theta_S \ . \end{cases} \tag{A31,32}$$

Defining the line-averaged square of the electron plasma frequency as

$$\Lambda_S\,\omega_{pS}^2 = 3.18 \times 10^3\,N_{eS}, \tag{A33,34}$$

this contribution to the optical depth is then

$$\alpha_{eaS}\,\Lambda_S = \frac{\Lambda_S\,\omega_{pS}^2}{\omega^2}\,\frac{\nu_S}{c}. \tag{A35,36}$$

Combining the previous quantities, the total optical depth is

$$\alpha_S \Lambda_S = \left(\alpha_{eiS} + \alpha_{fbS} + \alpha_{eaS}\right)\Lambda_S. \tag{A37,38}$$

This last quantity applies to photon transport "forward" or "backward" through the thickness of the vapor zone, i.e., normal to the material surface. In addition, each zone can radiate radially, "sideways" through the cylindrical cross-section, and this optical depth is given by $\alpha_S d$.

An ideal black body radiates a spectral power density

$$B_S(\eta) = A\,\theta_S^4\,\eta_S^3\left[\exp(\eta_s) - 1\right]^{-1} \tag{A39,40}$$

where $A = 1.5809 \times 10^8$ W/m^2/(eV^4). For a uniform medium, the equation of radiative transfer yields the forward/backward and sideways spectral emissivities, respectively,

$$e_S(\eta) = B_S(\eta)\left[1 - \exp(-\alpha_S \Lambda_S)\right] \tag{A41,42}$$

$$e_{S2D}(\eta) = B_S(\eta)\left[1 - \exp(-\alpha_S d)\right]. \tag{A43,44}$$

Photons emitted from the source vapor towards the material surface are only partly transmitted through the target vapor, and the resulting target spectral transmission to the surface is

$$t_T(\eta) = e_S(\eta)\exp(-\alpha_T \Lambda_T). \tag{A45}$$

Similarly, a small amount of the target emission is transmitted through the source vapor, backward towards the external power source:

$$t_S(\eta) = e_T(\eta)\exp(-\alpha_S \Lambda_S). \tag{A46}$$

34

The spectral emissivities and transmission are functions of wavelength, and the associated power densities are gotten by integrating over all wavelengths; in practice we integrate over $0 \leq \eta_s \leq 10$.

source backward radiated power density $P_{SB} = \int_0^\infty d\eta \left(e_S + t_S \right)$ (A47)

source sideways radiated power density $P_{S2D} = \int_0^\infty d\eta \, e_{S2D}$ (A48)

net source to target radiated power density $P_{SF} = \int_0^\infty d\eta \left(e_S - e_T \right)$ (A49)

target forward radiated power density $P_T = \int_0^\infty d\eta \left(e_T + t_T \right)$ (A50)

target sideways radiated power density $P_{T2D} = \int_0^\infty d\eta \, e_{T2D}$ (A51)

The various energy density fluences normal to the surface are:

kinetic energy external input to source vapor $U_1 = \int_0^t q_0 \, dt$ (A52)

photon radiation loss backward $U_2 = \int_0^t P_{SB} \, dt$ (A53)

photon radiation loss forward to surface $U_3 = \int_0^t P_T \, dt$ (A54)

kinetic energy input to target by vaporized atoms $U_4 = N_T \dfrac{3}{2} \varepsilon \, \theta_{T_0}$ (A55)

net energy transfer from source to target vapor $U_9 = \int_0^t P_{SF} \, dt$. (A56)

The sideways radiated power is an additional energy sink, and, normalized to the cross-sectional area of the external power source ($\pi d^2/4$), these energy losses are

source sideways radiation $\qquad U_5 = \dfrac{\Lambda_S \, \pi \, d}{\pi \, d^2/4} \displaystyle\int_0^t P_{S2D} \; dt \qquad$ (A57)

target sideways radiation $\qquad U_6 = \dfrac{\Lambda_T \, \pi d}{\pi \, d^2/4} \displaystyle\int_0^t P_{T2D} \; dt. \qquad$ (A58)

Additional energy sinks are associated with vapor particle losses if the vapors expand far enough to contact materials surfaces (e.g., when $\Lambda_S + \Lambda_T > d_G$):

source loss $\qquad\qquad\qquad U_7 = \displaystyle\int_0^t \dot{K}_S \; dt \qquad$ (A59)

target loss $\qquad\qquad\qquad U_8 = \displaystyle\int_0^t \dot{K}_T \; dt. \qquad$ (A60)

Energy conservation dictates that the source vapor stores an energy density

$$U_S = U_1 - U_2 - U_5 - U_9 - U_7 \;, \qquad (A61)$$

and the target vapor's energy density is

$$U_T = U_9 + U_4 - U_3 - U_6 - U_8 \;. \qquad (A62)$$

Particle loss from the vapor columns is treated in the simplest possible manner. First, the sum of the vapor zone thicknesses, $\Lambda_\Sigma \equiv \Lambda_S + \Lambda_T$, is monitored. If $\Lambda_\Sigma \leq d_G$ no particle loss occurs. Otherwise, the line average densities, N_S' and N_T', are reduced to yield

$$N_S = \frac{d_G}{\Lambda_\Sigma} N_S'$$

and

$$N_T = \frac{d_G}{\Lambda_\Sigma} N_T' .$$

For a given time step, Δt, in the code, the loss rates are

$$\dot{L}_S = \left(N_S' - N_S \right) / \Delta t \tag{A63}$$

$$\dot{L}_T = \left(N_T' - N_T \right) / \Delta t. \tag{A64}$$

This loss algorithm does not affect the density or pressure of the vapors. Associated with the particle loss is the kinetic energy loss:

$$\dot{K}_S = \dot{L}_S \frac{3}{2} \varepsilon \, \theta_S \left(1 + \Phi_S \, Z_S \right) \tag{A65}$$

$$\dot{K}_T = \dot{L}_T \frac{3}{2} \varepsilon \, \theta_T \left(1 + \Phi_T \, Z_T \right) . \tag{A66}$$

The state variables, effective charge and degree of ionization, are functions of temperature and density. For the source plasma the electron density is (with analogous target vapor expressions)

$$n_{eS} = \Phi_S \, Z_S \, n_S . \tag{A67,68}$$

A fully ionized plasma ($\Phi \equiv 1$) has an effective charge Z_S given by

$$\chi_a \left(Z_S + 1/2 \right) = \theta_S \, \ell n \left[\frac{6.04 \times 10^{27} \, \theta_S^{1.5}}{n_{eS}} \right] \tag{A69,70}$$

where χ_a is the piecewise continuous extension of the ionization potential. (This expression applies to non-hydrogen plasma, since $Z_S \equiv 1$. for hydrogen.) If this expression yields Z_S greater than Z_{Max}, the atomic number of the element, the result is replaced with $Z_S = Z_{Max}$. Partially ionized plasma has $Z_S \equiv 1$., and the degree of ionization is given by

$$\left\{ \frac{n_{iS}}{n_{aS}} \equiv r_s = \sqrt{\frac{6. \times 10^{27}}{n_{aS}}} \; \theta_S{}^{0.75} \exp\left[-\chi_{S1}/(2\,\theta_S)\right] \right. \tag{A71,72}$$

$$\left\{ \Phi_S = r_S/(1+r_S) \right. \tag{A73,74}$$

Here χ_{S1} is the first ionization potential of the neutral atom. At a given plasma density these expressions are solved for Z_S and Φ_S over a wide range of θ_S values. In these transcendental equations $n_{eS} = n_{eS}(Z_S)$ and $n_{aS} = n_{aS}(\Phi_S)$; solutions are obtained by iteration until convergence is achieved.

At each time step the temperature and state variables are updated by equating the energy density per particle density to the vapor's heat capacity,

$$U_S/N_S = \varepsilon\, c_S(\theta_S, n_S). \tag{A76,77}$$

The heat capacity (eV per nucleus) is

$$c_S = \frac{3}{2}\,\theta_S\left(1. + \Phi_S\, Z_S\right) + \Phi_S\, \sigma_S(Z_S). \tag{A78,79}$$

The first term in c_S is the sum of the nucleus and free electron kinetic energies, and σ_S is a continuous function of Z_S, which equals the sum of the ionization potentials at that Z_S. For example, for an Fe plasma with $Z = 3.0$, $\sigma = \chi_{Fe1} + \chi_{Fe2} + \chi_{Fe3}$. Linear and quadratic interpolation and extrapolation are used to fit σ to the first nine ionization potentials. This second term represents the excitation and ionization energy stored in the plasma; and σ has its upper bound when $Z = Z_{Max}$.

The code also monitors the vapor densities to confirm that the plasmas are in the Saha regime. That is, we require throughout that

$$n_e > 1. \times 10^{22}\, \theta^{3.5}.$$

38

Finally, the line average density of the target vapor is found from the vaporization rate, $f(P_T)$, as

$$N_T = \int_0^t f(P_T)\, dt - \int_0^t \dot{L}_T\, dt. \tag{A80}$$

The first integrand is a function of the radiated power density reaching the material surface, and the second term represents particle losses. The integrated energy transmission fraction through the two vapors is

$$Y = U_3/U_1 \, , \tag{A81}$$

and the erosion depth of the surface is

$$\delta = \int_0^t f(P_T)\, dt/\rho \, . \tag{A82}$$

DISTRIBUTION LIST FOR ANL/FPP/TM-268

Internal

H. Attaya	H. Herman	K. Natesan	TIS Files
M. Billone	T. Hua	L. Neimark	
J. Brooks	C. Johnson	J.-H. Park	
O. Chopra	T. Kassner	B. Picologlou	
H. Chung	K. Kasza	C. Reed	
D. Diercks	J. Kopasz	D. Smith	
D. Ehst	A. Krauss	D.-K. Sze	
Y. Gohar	L. LeSage	S.-W. Tam	
I. Gomes	S. Majumdar	H. Tsai	
D. Gruen	S. Malang	L. Turner	
A. Hassanein	R. Mattas	FPP Files (30)	

External

DOE-OSTI, for distribution per UC-423 (48)
Manager, Chicago Operation Office
ANL-E Libraries (2)
ANL-W Library
W. Bauer, Sandia Laboratories, Livermore
R. Bastasz, Sandia Laboratories, Livermore
D. Buchenauer, Sandia Laboratories, Livermore
R.B. Campbell, Sandia Laboratories, Albuequerque
S.A. Cohen, Princeton Plasma Physics Laboratory
R. Conn, University of California, Los Angeles
D.L. Cook, Sandia National Laboratories, Albuquerque
T. Dolan, Idaho National Engineering Laboratory
W. Dove, U.S. Department of Energy
J. Gahl, University of New Mexico
W. Gauster, ITER, Garching Co-Site
J. Gilligan, North Carolina State University
D. Hill, General Atomics
Y. Hirooka, University of California, Los Angeles
I. Hutchinson, Massachusetts Institute of Technology
S. Jardin, Princeton Plasma Physics Laboratory
A. Kellman, General Atomics
C. Kessel, Princeton Plasma Physics Laboratory
B. Lipschultz, Massachusetts Institute of Technology
J. MacFarlane, University of Wisconsin
J. McDonald, Sandia Laboratories, Albuquerque
R. McGrath, Sandia Laboratories, Albuquerque
B. Merrill, Idaho National Engineering Laboratory
F. Najmabadi, University of California, Los Angeles
W. Nevins, Lawrence Livermore National Laboratory
R. Nygren, Sandia Laboratories, Albuquerque
R.R. Parker, ITER, Garching Co-Site

P. Parks, General Atomics
R.R. Peterson, University of Wisconsin
D. Post, ITER, San Diego Co-Site
P. Rockett, Sandia Laboratories, Albuquerque
A.J. Russo, Sandia Laboratories, Albuquerque
N. Sauthoff, Princeton Plasma Physics Laboratory
R.O. Sayer, Fusion Engineering Design Center/ORNL
W.M. Stacey, Georgia Institute of Technology
M. Ulrickson, Sandia Laboratories, Albuquerque
P. Wang, University of Wisconsin
R.D. Watson, Sandia Laboratories, Albuquerque
W.P. West, General Atomics
K. Wilson, Sandia Laboratories, Livermore
C. Wong, General Atomics

END

DATE FILMED

2 / 17 / 94